Heliyon 9 (2023) e12812

Contents lists available at ScienceDirect

Heliyon

journal homepage: www.cell.com/heliyon

Research article

Numerical prediction of transient electrohydrodynamic instabilities under an alternating current electric field and unipolar injection

Chu-Tong Zhou [a,b], Zhen-Ze Yao [a,b], Di-Lin Chen [a,b], Kang Luo [a,b,**], Jian Wu [a,b], Hong-Liang Yi [a,b,*]

[a] School of Energy Science and Engineering, Harbin Institute of Technology, Harbin, 150001, People's Republic of China
[b] Key Laboratory of Aerospace Thermophysics, Harbin Institute of Technology, Harbin, 150001, People's Republic of China

ARTICLE INFO

Keywords:
Electroconvection
Alternating current
Electrohydrodynamic
Instability and bifurcation

ABSTRACT

In this paper, a direct numerical simulation (DNS) of dielectric fluid flow subjected to unipolar injection under an alternating current (AC) electric field is carried out. The effect of frequency f of pulsed direct current (PDC) and AC on the transient evolution of electroconvection and their subcritical bifurcations are investigated in details. Electroconvection under PDC or AC tends to exhibit oscillating flow due to the periodic boundary condition of charge density and potential compared to the direct current (DC) case. The results demonstrate that under the PDC field, the linear criterion T_c decreases with increasing frequency, while the nonlinear stability criterion T_f is hardly affected. Under the AC field, a critical frequency $f_c = 0.0316$ is found, which separates electroconvection into two typical flow regimes—periodic flow regime ($f < f_c$) and inhibited flow regime ($f \geq f_c$)—depending on whether free charges can reach the collector electrode before electric field inversion. AC-electrohydrodynamics (EHD) systems promote various flow patterns with relatively lower voltage regimes than DC-EHD systems. These mechanisms of electroconvection under the PDC/AC field offer unique possibilities for fluid flow control in biological EHD-driven flow and portable EHD applications.

1. Introduction

EHD involves interdisciplinary research on hydrodynamic and electric fields. Electroconvection flow (ECF) induced by charge injection is an important subject in EHD. Under an external electric field, the electrodes inject charges. The Coulomb force acts on charges and causes the fluid to flow. Owing to its low noise and energy consumption and lack of mechanical movement, EHD technology has unique advantages in active flow control [1], microchannel transport [2], heat transfer enhancement [3], EHD drag pumps [4,5], alternating current (AC)–EHD fluid micromixing and microfluidic systems [6,7,8], EHD printing driven by pulsed and AC voltages [9,10,11], atomization technology [12], and so on.

Coulomb force-driven hydrodynamic instabilities, also called electroconvection flow (ECF) instabilities, are an important issue in EHDs and have drawn much attention in the past few decades [13]. Under an external applied direct current (DC) electric field, ECF is a

* Corresponding author. School of Energy Science and Engineering, Harbin Institute of Technology, Harbin, 150001, People's Republic of China.
** Corresponding author. School of Energy Science and Engineering, Harbin Institute of Technology, Harbin, 150001, People's Republic of China.
E-mail addresses: luokang@hit.edu.cn (K. Luo), yihongliang@hit.edu.cn (H.-L. Yi).

https://doi.org/10.1016/j.heliyon.2023.e12812
Received 27 September 2022; Received in revised form 26 December 2022; Accepted 3 January 2023
Available online 11 January 2023

subcritical bifurcation pattern. The feature of subcritical bifurcation refers to when the driving parameter T (representing the ratio of the destabilizing Coulomb force to the stabilizing viscous force) reaches the linear critical value T_c [14,15], the flow jumps from stationary to a regular convection state. When T is lower than another criterion T_f (the nonlinear criterion), the flow recovers back to a zero state [16]. Because the nonlinear criterion T_f is smaller than the linear criterion T_c, these two criteria form a hysteresis loop [16]. This subcritical ECF bifurcation with a hysteresis loop was proven in several later works [15,17,18,19] inside a model of an infinite layer of liquid between two parallel metal electrodes under a DC field. Félici et al. [18] used a hydraulic model to simplify ECF into a pair of two-dimensional (2D) vortices and first conducted a detailed theoretical analysis of the physical mechanism under a weak charge injection pattern. Atten and Lacroix [20,21] then optimized the model of Félici et al. to consider 2D vortex pairs as hexagonal cells and studied nonlinear instability problems. The presence of a nonlinear criterion and hysteresis loop related to discontinuities of current and fluid velocity was successfully predicted. Castellanos and Atten [22], Chicón et al. [23], Vázquez et al. [24,25,26], and Traoré et al. [16,26,27] confirmed the hysteresis loop via numerical and experimental methods [21]. Later, the effects of other factors, including the thermal effects [27], rigid wall effects [28], solid–liquid interface [29,30], injection configurations [three-dimensional (3D) and two coaxial cylinders] [31,32], and viscoelastic fluid [31,33] on flow structures and linear stability criteria were investigated numerically. Recently, Roy et al. [34] studied the effects of adding nanoparticles in EHD flows.

However, most existing works on electroconvective instabilities are based on DC assumptions. The unsteady AC field will introduce additional instabilities, increasing the complexity of the dynamic problem. The consideration of EHD under the AC/PDC field is necessary from the aspects of both fundamental physical study and application. At present, several important fundamental studies have numerically shown EHD-rich instabilities under an AC field; Smorodin et al. [35,36] pointed out that parameter modulation can induce parametric resonance that emerges in hydrodynamic systems. There are three possible patterns of responses. The subharmonic response is that the frequency (oscillation of the system characteristics) may be twice that of the external forcing. The second type is the synchronous response, which refers to when the frequency of oscillation flow coincides with the excitation period. A third type is that a flow oscillation has two no rationally related characteristic frequencies. It is a quasiperiodic response. Nevertheless, three still have some fundamental studies related to bifurcation that need to be explored in depth. Concurrently, EHD equipment under an AC field has a great advantage over a DC field, especially in EHD printing and biological EHD-driven fluid flow systems. Nguyen et al. [37] demonstrated that AC-EHD printing had advantages over DC in nozzle manufacturing, drop-on-demand capabilities and droplet repulsion according to the frequency f of the applied sinusoidal electric voltage. Kim et al. [38] performed EHD printing under a PDC field (square wave) and controlled the droplet size by changing the amplitude of the voltage. In biological EHD-driven fluid flow systems, AC-EHD systems are usually used in fluid handling compared to DC EHD systems due to (a) avoiding electrode damage or electrolysis and (b) the ability to operate at relatively low voltages, making AC-EHD systems appropriate for biological applications and portable systems [39]. Therefore, it is necessary to pay great attention to EHD problems under the AC field.

Previous studies on EHD under an AC field have mainly focused on nematic liquid crystals [40,41,42,43]. The anisotropic nature of these materials seemed to explain the mechanism of instability and various experimental observations. Electrokinetic flow under an AC field also exhibits many unique mechanisms that have been widely investigated [44,45,46,47,48]. Experimental, numerical, and theoretical studies on the electroconvection of dielectric liquids under AC and pulsed DC (PDC) electric fields are relatively limited. In a previous research, Atten extended earlier research on the DC ECF of two parallel electrodes into an AC field [49]. The effects of frequency f on the linear criterion are mainly studied. Smorodin et al. [50] focused on the thermoelectric instability under a periodically varying heat flux in a liquid semiconductor or an ionic melt layer. They found characteristics of critical disturbances and the boundaries of instability under the influence of thermoelectric, surface tension gradients and buoyancy. Additionally, Smorodin et al. [51] continued to focus on the electro-thermo convective instability of a poorly conducting horizontal liquid layer under a varying electric field. They studied the fluid instabilities influenced by a modulated electric field with and without the effect of buoyancy. In two recent studies, Nekrasov et al. [52] studied 2D nonlinear electroconvective patterns in the case of heating from above under DC and AC fields. They presented the bifurcation behavior of different solutions according to the electric Rayleigh number. Sun et al. [53] performed an experimental research on ECF under needle plate construction and compared the results of the DC and AC fields.

Therefore, we perform numerical simulations on the instability of EHD flows in a dielectric fluid subjected to unipolar injection under AC fields. In addition to the typical sinusoidal alternating current, PDC is also considered an intermediate step from the DC field to the AC field. The main objectives include two aspects: (1) to explore the relationship between the finite amplitude criterion (linear and nonlinear criterion) and frequency f and (2) to find the electroconvection structures under PDC and AC fields. In Section II, the description of the mathematical and physical model and the numerical methods are described, with a brief introduction to the finite volume method (FVM). In Section III, model validations are performed with two benchmarks. In Section IV, our numerical results are presented and discussed. Finally, conclusions are presented in Section V.

2. Problem formulation

A fluid layer (width H) enclosed by two parallel metal electrodes (length L) subject to a PDC or AC voltage difference is considered in this paper, as shown in Fig. 1. A (L/H) is the aspect ratio of our configuration. The potential of the bottom electrode is maintained at $\varphi_0 = |\varphi_{\max} \sin(2\pi ft)|$ for the PDC case or at $\varphi_0 = \varphi_{\max} \sin(2\pi ft)$ for the AC case. In contrast, the potential of the top electrode holds at φ_1. The fluid in our system is considered incompressible and completely insulating with constant physical properties. The three types of charge transportation are ionic drift, convection, and diffusion.

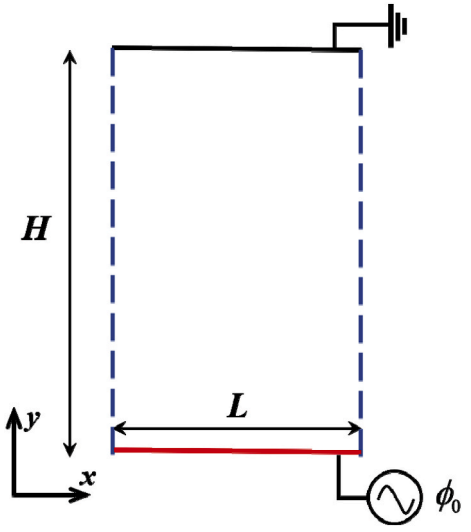

Fig. 1. Sketch of electrohydrodynamic system. The distance between two electrodes is characterized as H.

2.1. Base governing equations

The incompressible hydrodynamic equations [54] are the momentum Eq. (1) and the continuity Eq. (2),

$$\rho_0\left(\frac{\partial u}{\partial t}+u\cdot\nabla \mathrm{u}\right)=-\nabla \mathrm{p}+\eta\Delta u+f_e \tag{1}$$

$$\nabla\cdot\mathbf{u}=0 \tag{2}$$

where $\mathbf{u}$ is the fluid velocity field, p is the pressure, t is the time, η is the fluid dynamic viscosity, ρ_0 is the fluid density, and $\mathbf{f_e}$ is the density of the electric force. The electric force (3) that acts on a unit volume of the dielectric liquid can be written as [55]:

$$f_e=qE-\frac{E^2}{2}\nabla\varepsilon+\nabla\left[\frac{E^2}{2}\rho\frac{\partial\varepsilon}{\partial\rho}\right] \tag{3}$$

where q represents the charge density, $\varepsilon=\varepsilon_r\varepsilon_0$ represents the fluid permittivity, $\mathbf{E}$ represents the electric field, and ε_0 represents the vacuum permittivity. We have $\nabla\varepsilon=0$ in isothermal and homogeneous fluids, and the right second term of $\mathbf{f_e}$, that is, the dielectric force, vanishes. By including the right third term, the electrostriction force in the pressure gradient term $p+\left[\frac{\mathbf{E}^2}{2}\rho\frac{\partial\varepsilon}{\partial\rho}\right]=\widetilde{p}$, Eq. (1) can be simplified to Eq. (4)

$$\rho_0\left(\frac{\partial\mathbf{u}}{\partial t}+\mathbf{u}\cdot\nabla\mathbf{u}\right)=-\nabla\widetilde{p}+\eta\Delta\mathbf{u}+q\mathbf{E} \tag{4}$$

The electric field Eq. (5) and the Poisson Eq. (6) are given by

$$\mathbf{E}=-\nabla\varphi \tag{5}$$

$$\nabla\cdot(\varepsilon\nabla\varphi)=-q \tag{6}$$

where φ is the electric potential.

The conservation of charge density (7) is represented as follows:

$$\frac{\partial q}{\partial t}+\nabla\cdot\mathbf{j}=0 \tag{7}$$

Assuming a linear isotropic medium and the four classical distinct charge transport mechanisms—electroconvection, electromigration, diffusion, and conduction—we can show the expression of the current density $\mathbf{j}$ (8):

$$\mathbf{j}=q\mathbf{u}+qK\mathbf{E}-D\nabla q \tag{8}$$

where K and D are the ionic mobility and charge-diffusion coefficient, respectively. Since the fluid is considered isothermal, Joule heating and viscous dissipation are inappreciable. In fact, the current through the dielectric liquid is quite small. Therefore, magnetic field effects are usually ignored during numerical simulations. The diffusion current is considered here. Therefore, $\mathbf{j}$ consists of three

parts: conduction component $qK\mathbf{E}$ (ion electromigration), convection component $q\mathbf{u}$ (fluid flow) and diffusion component $-D\nabla q$ (ion diffusion).

2.2. Dimensionless parameters and equations

To make the described problem universal, we use nondimensional equations by introducing the dimensionless quantities (9) and (10), denoted with an asterisk:

$$x_i^* = \frac{x_i}{H}, \rho^* = \frac{\rho}{\rho_0}, q^* = \frac{q}{q_0}, u_i^* = \frac{u_i}{u_0}, t^* = \frac{t}{H/u_0}, f^* = \frac{f}{f_0} \tag{9}$$

$$p^* = \frac{p}{\rho_0 u_0^2}, \varphi^* = \frac{\varphi}{(\varphi_0)_{rms} - \varphi_1}, E_i^* = \frac{E_i}{E_0} = \frac{E_i H}{\varphi_{0rms} - \varphi_1} \tag{10}$$

In these equations, $x_i^*(i = x, y)$ represents the spatial coordinate in the x/y direction, and t represents time. $K((\varphi_0)_{rms} - \varphi_1)/H$ is the reference velocity u_0, $\varepsilon((\varphi_0)_{rms} - \varphi_1)/H^2$ is the charge density, $(\varphi_0)_{rms} - \varphi_1$ is the electric potential, and $(\varphi_0)_{rms}$ represents the root-mean-square (RMS) electric potential of φ_0. The time scale is the transit ionic time H/u_0 [56], and the frequency scale is the inverse of the transit ionic time.

For clarity, we remove the asterisk indicator, and the basic dimensionless EHD equations for Newtonian fluids are expressed as follows:

$$\nabla \cdot \mathbf{u} = 0 \tag{11}$$

$$\frac{\partial \mathbf{u}}{\partial t} + \mathbf{u} \cdot \nabla \mathbf{u} = -\nabla \widetilde{p} + \frac{M^2}{T} \nabla^2 \mathbf{u} + M^2 q \mathbf{E} \tag{12}$$

$$\frac{\partial q}{\partial t} + \nabla \cdot (q\mathbf{E} - \alpha \nabla q + q\mathbf{u}) = 0 \tag{13}$$

$$\mathbf{E} = -\nabla \varphi \tag{14}$$

$$\nabla^2 \varphi = -q \tag{15}$$

The dimensionless parameters in the above equations are as follows: $T = \varepsilon((\varphi_0)_{rms} - \varphi_1)/(\mu K)$ is the ratio of the Coulomb force and viscous force. $C = q_0 H^2/\varepsilon((\varphi_0)_{rms} - \varphi_1)$ is the injection level. $M = (\varepsilon/\rho_0)^{1/2}/K$ is the dimensionless mobility number that is calculated by the so-called hydrodynamic mobility of ions and the ions' true mobility. $\alpha = D/K((\varphi_0)_{rms} - \varphi_1)$ is the dimensionless diffusion number that represents the scale of charge diffusion and charge drift. We can find comprehensive descriptions of related physical equations and parameters in Refs. 55 and 57.

Our system has a particular time - ionic transit time t_T. $t_T = H/u_0 = H/KE$ represents the time of ions from one metal electrode to another under the action of a constant and uniform electric field. Thus, the characteristic frequency $f_c = 1/t_T = 0.0316$. We have an assumption that each electrode injects unipolar ions (cations) into the insulating liquid in one half of the cycle and collects those cations in the other half of the cycle for our AC electrodynamics system. For a system frequency greater than f_c, the ions cannot reach the other electrode during the half-cycle, which separates into two regimes: the periodic electroconvective flow regime ($f < f_c$) and the inhibited electroconvective flow regime ($f \geq f_c$).

2.3. Numerical implementation and boundary conditions

We need to give initial conditions because our system is time dependent. In general, we either start with a fluid at rest or with a steady state from previous simulations. Under an electric field, a thin electric double layer (EDL) [58] will form at the charged surfaces. The size of the EDL [58] is λ_D (16):

$$\lambda_D = \sqrt{\frac{\varepsilon k_b \theta}{2(ze)^2 c_0}} \tag{16}$$

where e represents elementary charge, z represents ionic valence, k_b represents Boltzmann constant, c_0 represents charge concentration of the injection electrode and θ represents temperature.

A common concentration $c_0 = o(10^{-5})$ results in $\lambda_D = o(10^{-3})$ in this paper, and the size of system H is $o(1)$. Therefore, the influence of the EDL on flow can be neglected in our work, and the boundary conditions on each boundary for the governing Eqs. (11), (12),(13),(14),(15) are described as follows:

In both PDC and AC cases, the symmetrical boundary conditions (17) for velocity, cations, pressure, and potential have been considered on the lateral borders:

$$u=0\ ,\quad \frac{\partial v}{\partial x}=0\ ,\quad \frac{\partial \varphi}{\partial x}=0\ ,\quad \frac{\partial q}{\partial x}=0\ ,\quad \frac{\partial \widetilde{p}}{\partial x}=0 \tag{17}$$

The boundary for velocity, the bottom and top solid electrodes are solved by the no-slip and no-penetration conditions (18),

$$y=0,H\quad \mathbf{u}=\mathbf{0} \tag{18}$$

For the potential of PDC or AC cases, because a PDC or AC potential difference is used, conditions (19) for both electrodes are given as

$$\begin{gathered} y=0,\varphi_0=|\varphi_{\max}\sin(2\pi ft)|\ \text{ for the PDC case};\quad \varphi_0=\varphi_{\max}\sin(2\pi ft)\ \text{ for the AC case} \\ y=H,\varphi_1=0\ \text{ for both the PDC and AC} \\ \text{cases} \end{gathered} \tag{19}$$

The boundary for charge density follows the injection law, a simplified formula [13] (20) that can be used for a wide range of dielectric liquids for the injection charge density q:

$$q=\frac{q_{i0}}{bK_1(b)} \tag{20}$$

where q_{i0} represents the charge density injected by electrodes at zero field, K_1 represents the second kind and first order of the modified Bessel function, and q represents the charge injection intensity of one single type ion. $bK_1(b)$ (21) can be expanded as follows [59]:

$$bK_1(b)=1+\frac{1}{2}b^2\ln(b/2)+\left(\frac{\gamma_E}{2}-\frac{1}{4}\right)b^2+\ldots \tag{21}$$

where γ_E represents the Euler constant: $\gamma_E=0.5772$, $b=l_b/l_o$, with the Bjerrum distance and Onsager distance (22) given as follows [57,60]:

$$l_B=e^2\Big/4\pi\varepsilon k_B\theta,\ l_o=\sqrt{e/4\pi\varepsilon|\mathbf{E}|} \tag{22}$$

where $b^2=4\gamma E$ and $\gamma=e^3/16\pi\varepsilon k_b^2\theta^2$ are the Onsager constants and $|\mathbf{E}|$ represents the electric intensity.

This means that q follows the injection law at the injector. From (20), we find that the injection density is affected by $|\mathbf{E}|$ and the liquid motion with time so that these models are more accurate than the *autonomous* injection condition that is widely used in most DC studies [31,32,33].

For the charge density (23) of PDC cases:

$$y=0,q=\frac{q_{i0}}{bK_1(b)};\quad y=H,\frac{dq}{dy}=0 \tag{23}$$

For the charge density (24a, 24b) of AC cases:

$$y=0,q=\frac{q_{i0}}{bK_1(b)};\quad y=H,\frac{dq}{dy}=0\ \text{(positive cycle of AC)} \tag{24a}$$

$$y=0,\frac{dq}{dy}=0;\quad y=H,q=\frac{q_{i0}}{bK_1(b)}\ \text{(negative cycle of AC)} \tag{24b}$$

For the pressure (25) of PDC and AC cases:

$$y=0,H\quad n\cdot\nabla\widetilde{p}=0 \tag{25}$$

Because the partial differential Eqs. (9),(10),(11),(12),(13) are very complex and highly nonlinear, most problems cannot be solved analytically. Therefore, we conduct numerical research through the FVM in OpenFOAM®, which has high stability and calculation efficiency. Furthermore, the semi-implicit method for pressure-linked equations–consistent (SIMPLEC) algorithm [61] is applied for coupling pressure and velocity. Euler discrete is applied for discretizing time variables. At the same time, the gradient term applied a Gaussian linear formula. To discretize the diffusion term, we use a second-order central difference (CD) scheme. The convection term of the charge transport equation is discretized by the convergent and universally bounded interpolation scheme for the treatment of advection (CUBISTA) scheme [62].

2.4. Model verification

Although complete mathematical frameworks have been established, we still need to verify the correctness of our models and codes through two sections.

First, we run direct numerical simulation (DNS) in the hydrostatic regime to research charge density features. The relevant results are also validated with the analytical data of Ref. 63 and Refs. [64], [65] in which the lattice Boltzmann method (LBM) is used. The performance of our adopted methodology is satisfactory, with the numerical solution agreeing well with the analytical solution (Fig. 2

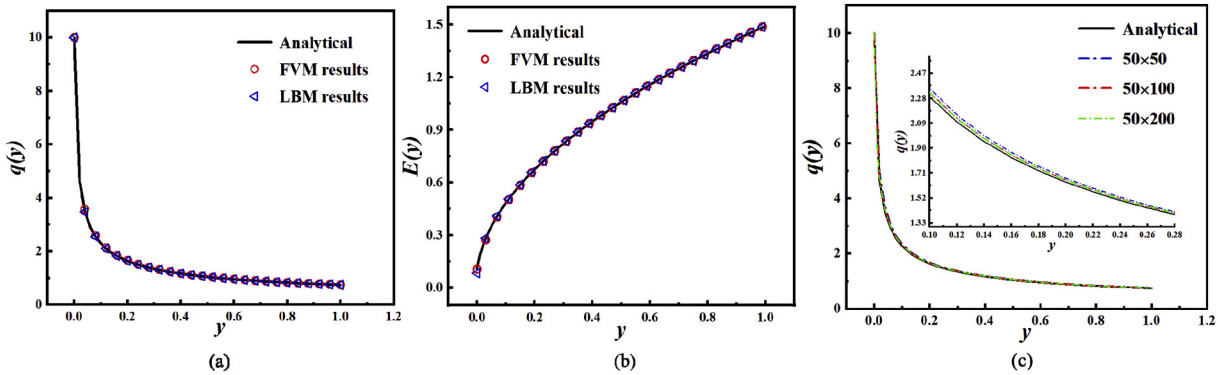

Fig. 2. Numerical results and analytical results along the y direction ($C = 10$) for the (a) charge density profile, (b) electric field profile and (c) grid independence tests.

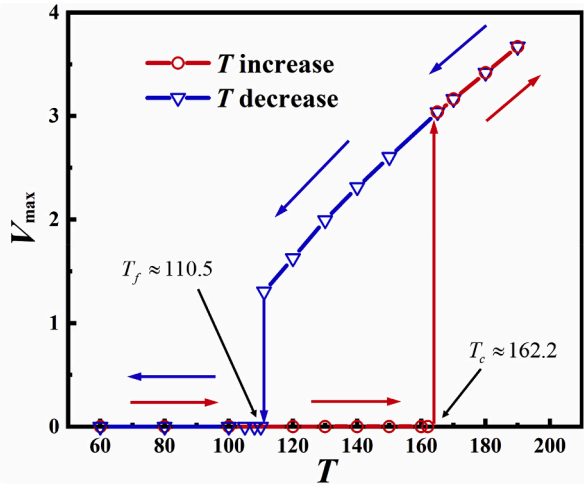

Fig. 3. Bifurcation diagram for $C = 10$, $M = 10$, and $\alpha = 1 \times 10^{-4}$ in the DC cases.

(a) (b)). Fig. 2(c) presents the charge density in the y direction for different grid sizes: 50×50, 50×100, and 50×200. The calculation results show that our numerical and analytical results match very well, even under the coarsest mesh (50×50). The grid size 50×200 is selected in this paper.

Since there are few results for PDC and AC–ECF, we repeated the well-established 2D DC flows [16,26] to verify our numerical model.

In Fig. 3, we show the bifurcation diagram obtained from our code. The bifurcation pattern of ECF is subcritical, with the hysteresis loop of linear criterion T_c and nonlinear criterion T_f. The results of T_c and T_f we calculate are 162.2 and 110.5, respectively. The linear criterion should be compared with 162.6 obtained from linear stability analysis [63]. The nonlinear criterion should be compared with 111.7 determined by the FVM method [18].

3. Results and discussion

Next, different flow patterns and their subcritical bifurcations for different T and frequencies of PDC and AC fields are investigated, and the numerical results are analyzed. We fix some dimensionless parameters in our work: $C = 10$, $M = 10$, and $\alpha = 1 \times 10^{-4}$.

Theoretical work determined that the critical wavelength λ_c, corresponding to the most unstable mode at the linear criterion T_c, can be minimized [21,63]. We conduct a series of numerical tests to determine λ_c for the PDC and AC electric fields by changing the wavelength λ and calculating the corresponding T_c. Fig. 4(a and b) shows the variation of T_c with wavelength λ under PDC ($f = 0.02$) and AC ($f = 0.01$) fields. In these computations, periodic boundary conditions have been used for the lateral walls. T_c reaches its minimum at $\lambda = 1.228$ for PDC and AC fields in the range of the numerical tests. Concurrently, the calculated results at $\lambda_c = 1.228$ have symmetry. Therefore, we can select half of the critical wavelength as the computational domain $L = 0.614$ ($A = 0.614$) for three typical waveforms (DC, PDC, and AC voltages) to reduce the computational load.

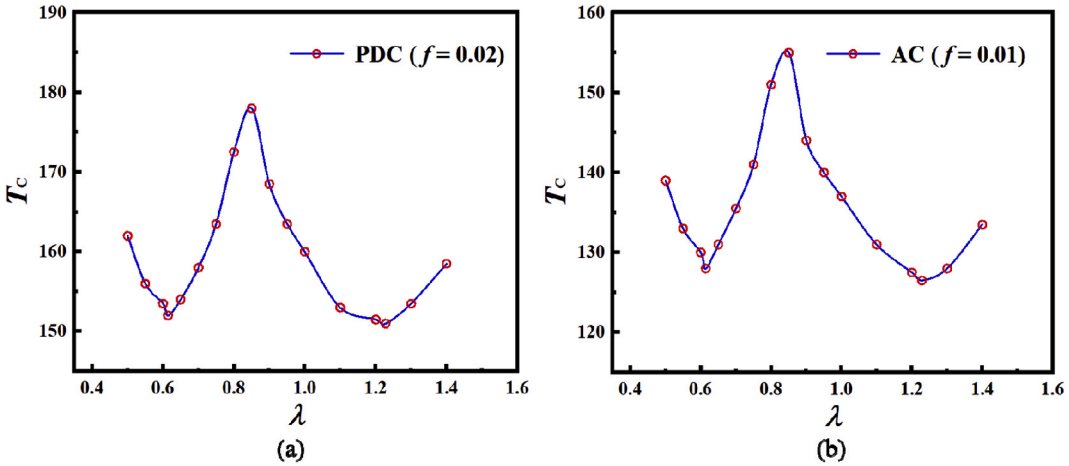

Fig. 4. T_c vs wavelength λ for $C = 10$ and $M = 10$. Periodic boundary conditions were applied to the lateral walls. (a) PDC field ($f = 0.02$) and (b) AC field ($f = 0.01$).

3.1. Stability for pure unipolar injection under DC and PDC fields

3.1.1. Electrodynamic structures

We first compare the temporal evolution of $V_{\max}$ and EHD structures between DC and PDC fields. Fig. 5(a) presents the temporal evolution of the corresponding $V_{\max}$ ($V_{\max} = \max(\sqrt{u^2 + v^2})$) under the DC and PDC fields for $T = 170$, which is higher than the critical value T_c. A similar evolution of fluid motion under a DC field can be observed. In the initial stage, the periodic disturbance accumulates slowly. When the disturbance accumulates to a certain extent, the fluid motion goes through stages of rapid development, and the velocity amplitude increases exponentially. Eventually, the flow evolves into a periodic steady flow. In contrast to the DC case [66], oscillations occur throughout PDC evolution. The peak value and RMS for the nondimensional maximum velocity of PDC electroconvection are 4.462 and 2.45, respectively. The nondimensional maximum velocity of DC electroconvection is 3.17 between the peak and RMS values of PDC. From Fig. 5(b), we can see that the peak of PDC is $\sqrt{2}$, which is higher than the 1 of DC. One possible reason why the RMS value of PDC is lower than the maximum value of DC is that the external electric field varies periodically from zero to peak over time [Fig. 5(b)] and cannot provide a steady driving force (qE), unlike the DC field. The other possible reason is that periodic variation of the flow field produces energy dissipation because the DC voltage is the same as the RMS of the PDC voltage.

ECF by an external DC field presents classical qualitative characteristics that are one convective cell structure and void charge region when $T = 170$. A similar result can be found for the present configuration when a PDC voltage is used. Fig. 6(a) presents the instantaneous distribution of the charge density and streamlines corresponding to five distinct times in an oscillation period. The top electrode is grounded, while the bottom electrode is positively charged. From Fig. 6(c), we can see that the external voltage at the

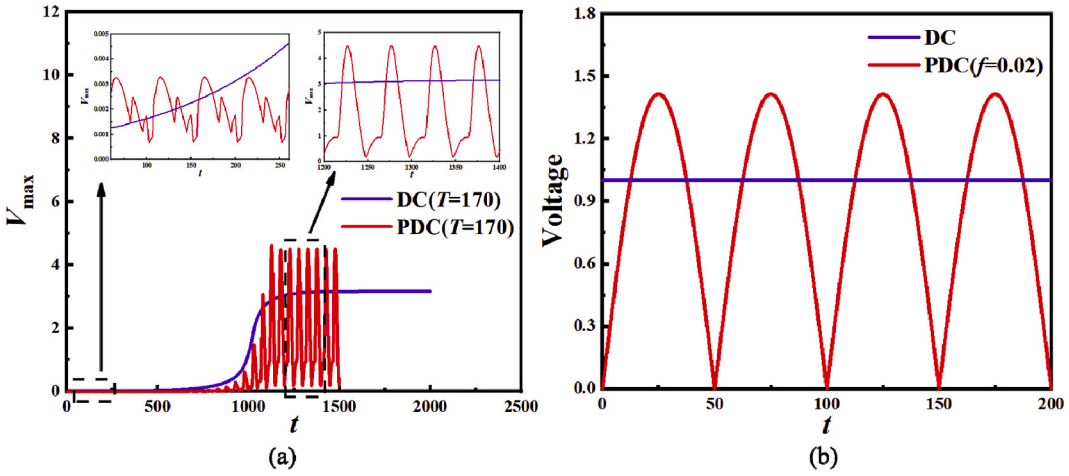

Fig. 5. (a) Temporal evolution of $V_{\max}$ for $T = 170$ in the direct current (DC) and pulsed direct current (PDC) ($f = 0.02$) cases and (b) external voltage variations of PDC ($f = 0.02$) and DC with time.

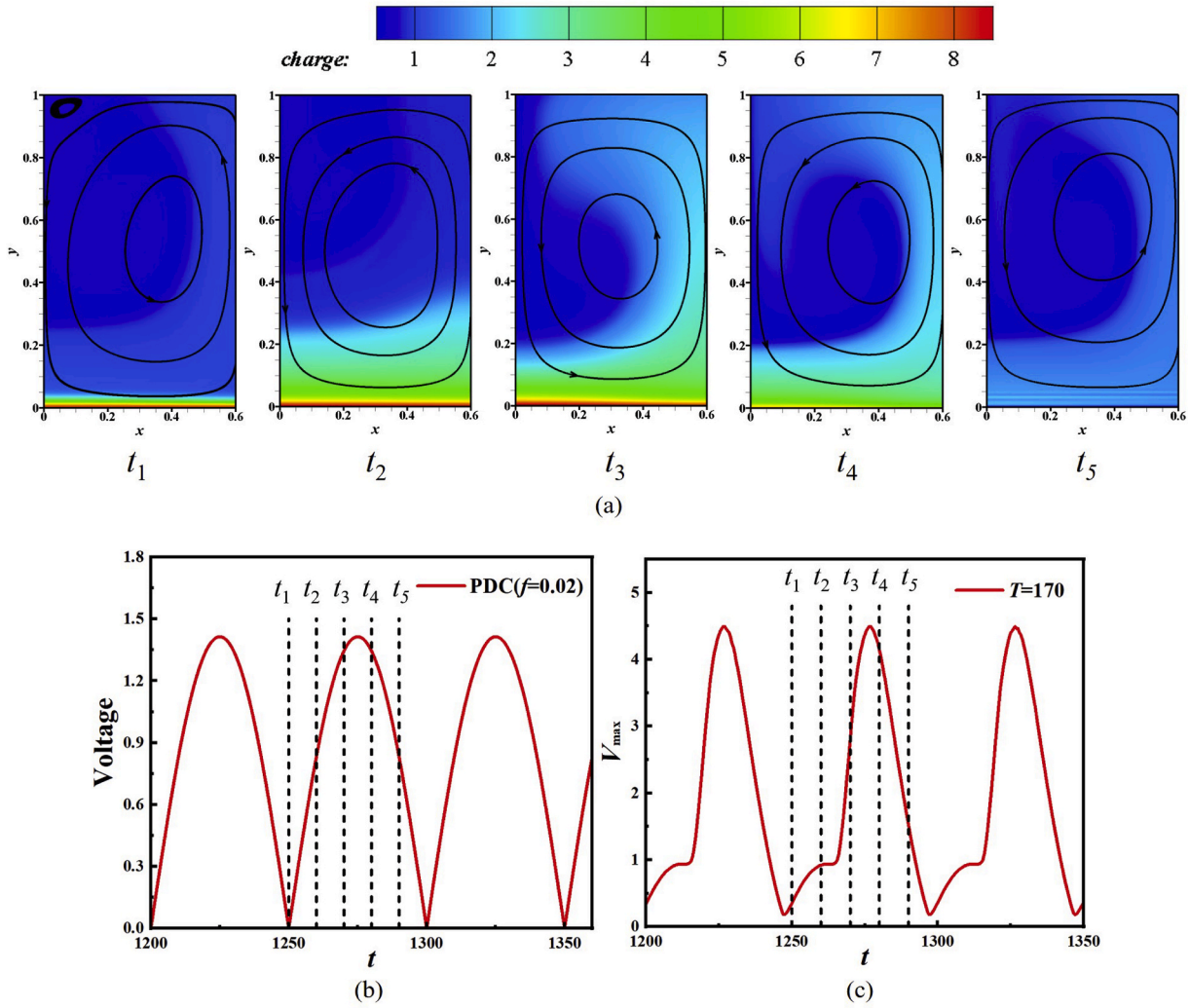

Fig. 6. Temporal evolution of charge density q distribution, voltage and maximum velocity (V_{max}) for $T = 170$ and $f = 0.02$, as a representative of the regular oscillation: (a) charge density distribution and streamlines at five distinct times, (b) external periodic voltages of pulsed direct current ($f = 0.02$) and (c) the periodic V_{max} signal.

bottom electrode reaches its maximum V_{max} between t_3 and t_4. The PDC frequency is $f = 0.02$, which is below the characteristic frequency of this system.

When the instantaneous voltage on the channel increases [Fig. 6(b) between t_1 and t_2], a charge layer comparable to 1/3 of the channel height is formed. When the voltage continues to increase [Fig. 6(b) between t_2 and t_3], the typical void charge region is initially formed. At the maximum voltage difference [Fig. 6(b) between t_3 and t_4], the complete void charge region is observed. Similarities to the findings of Wu [66] are observed under the DC field. When the voltage difference drop returns back to zero in Fig. 6(b) between t_4 and t_5, the void charge region is relaxed primarily because of a significant decrease in velocity and charge diffusion.

Figs. 5 and 6 mainly consider the effect of PDC on ECF for low values of T. We also consider the corresponding results for $T = 400$ under PDC, which has different flow structures than those at $T = 170$ because the second bifurcation occurs [16].

Fig. 7 presents the V_{max} temporal evolution for the DC and PDC cases for $T = 400$. For the PDC case, the flows first show a one-cell structure that is similar to Fig. 6(a), and then after experiencing a transition stage, a two-cell structure with lower values of V_{max} occurs. Additionally, the velocity oscillates periodically throughout the whole process. The steady-state nondimensional maximum velocity of DC electroconvection is 4.21. The peak value and RMS of the steady-state nondimensional maximum velocity of PDC electroconvection are 7.12 and 3.75, respectively. The possible reasons are similar to those outlined for the $T = 170$ case.

Similar processes as the case for $T = 170$ are observed at $T = 400$ under the PDC field. When the instantaneous voltage on the channel increases [Fig. 8(a) between t_1 and t_2], the maximum velocity V_{max} increases slowly [Fig. 8(b) between t_1 and t_2]and a charge layer comparable to 1/10 of the channel height is formed [Fig. 8(c) between t_1 and t_2]. When the voltage continues to increase [Fig. 8 (a) between t_2 and t_3], V_{max} increases rapidly [Fig. 8(b) between t_2 and t_3], the typical void charge region is formed initially, and

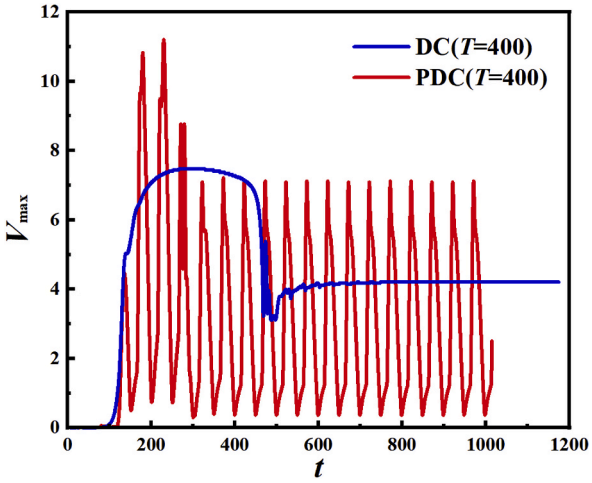

Fig. 7. Temporal evolution of V_{max} for $T = 400$ in the direct current and pulsed direct current ($f = 0.02$) cases.

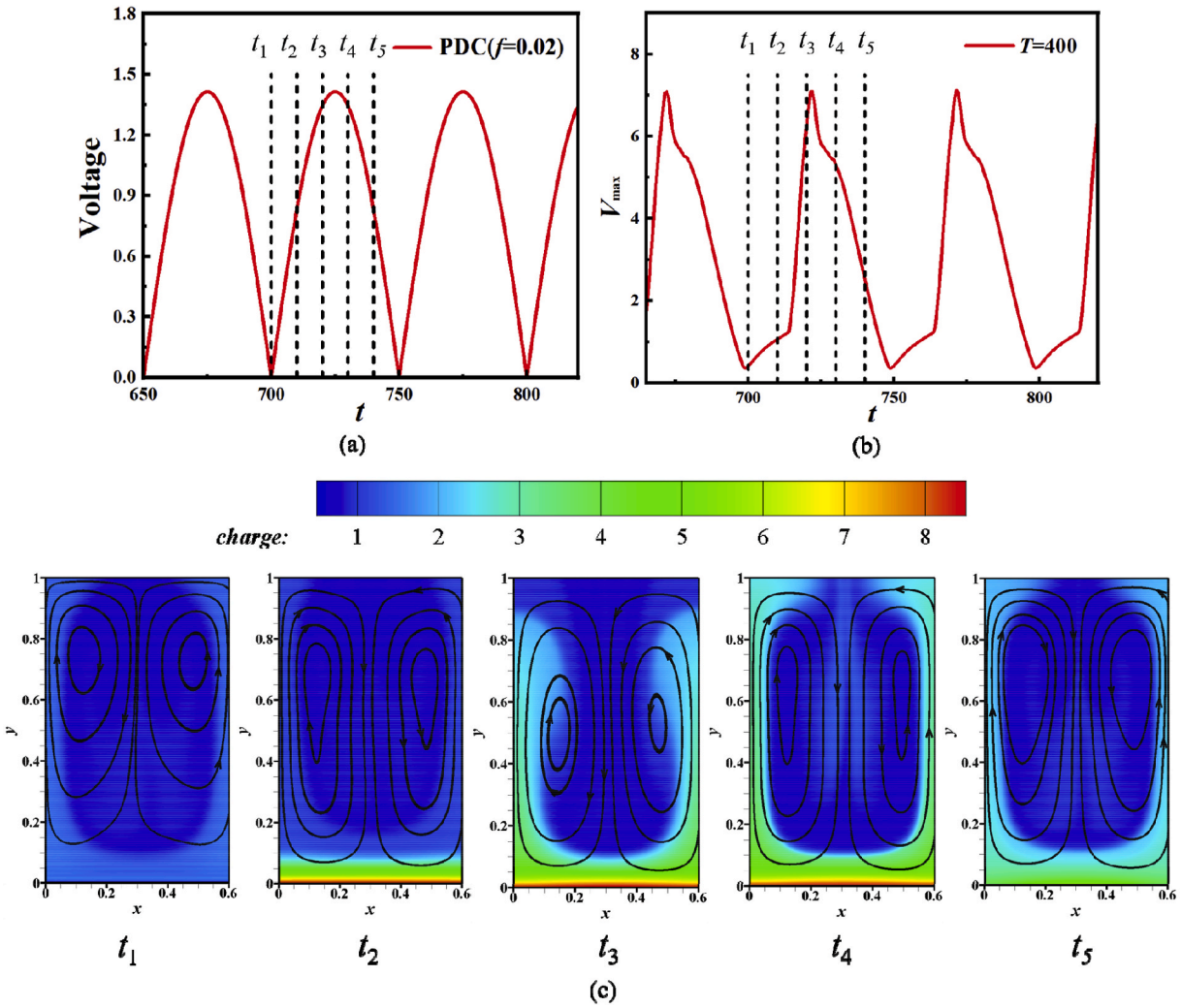

Fig. 8. Temporal evolution of voltage, V_{max}, charge density, q, distribution ($T = 400$ and $f = 0.02$), as a representation of the regular oscillation: (a) external periodic voltages of pulsed direct current ($f = 0.02$), (b) the periodic V_{max} signal and (c) charge density distribution and streamlines at five distinct times.

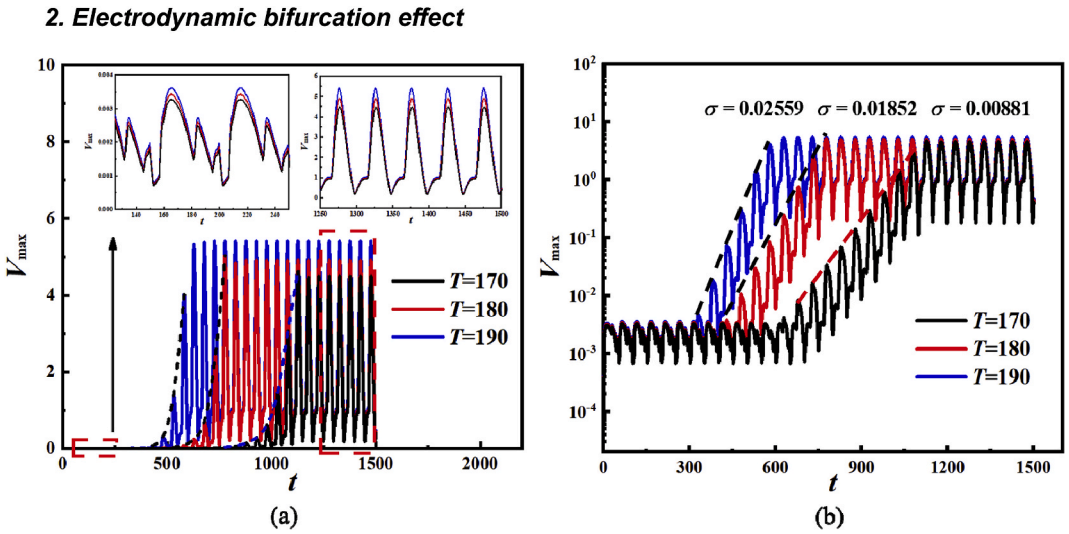

Fig. 9. Evolution of V_{max} for $C = 10$ and $M = 10$ in the pulsed direct current ($f = 0.02$) field; cases for $T = 170$, $T = 180$, and $T = 190$.

charges are injected into the bulk region from both sides of the edge [Fig. 8(c) between t_2 and t_3]. At the maximum voltage difference [Fig. 8(a) between t_3 and t_4], V_{max} reaches its peak [Fig. 8(b) between t_3 and t_4], and a complete void charge region is observed in the middle of the domain [Fig. 8(c) between t_3 and t_4], similar to the findings of Wu [66]. When the voltage drop returns back to zero in Fig. 8(a) between t_4 and t_5, V_{max} declines [Fig. 8(b) between t_4 and t_5], and the void charge region is also relaxed [Fig. 8(c) between t_4 and t_5], primarily because of the decrease in velocity and charge diffusion.

3.1.2. *Electrodynamic bifurcation effect*

Bifurcation is a characteristic feature in electroconvection that most experimental and numerical studies have focused on [16,63,66]. Therefore, this section discusses the subcritical bifurcation in ECFs under DC and PDC fields. We first briefly introduce a common way to obtain the linear criterion T_c from numerical calculations of DNS [67]. Theoretically, when T reaches approximately the linear instability threshold, the perturbations of each physical quantity f follow: $f = f_0 e^{\sigma t}$, where σ is the growth rate. We can calculate the growth rates from V_{max} evolution curves over time under several T. Then, we can calculate the linear criterion T_c, which corresponds to $\sigma = 0$ by extrapolation. We present the peak velocity V_{max} evolution curves over time for $T = 170$, $T = 180$, and $T = 190$ under the PDC ($f = 0.02$) field in Fig. 9(a and b). The exponential behavior is visually seen from the semilog plot [Fig. 9(b)]. The growth rates were determined by linear fitting during the exponential growth stage. For each of the three cases, our numerical prediction of T_c is approximately 152.

Fig. 10(a and b) describe the complete bifurcation diagram of the DC case and PDC case with $f = 0.02$. When the flow field starts from a hydrostatic solution, the flow remains static as we increase the driving parameter T. When T approaches 152, there is a sudden change in velocity, which exhibits the subcritical bifurcation characteristic that is typical for electroconvection. We found that the linear criterion T_c of the PDC case ($f = 0.02$) is lower than that of the DC case and that the nonlinear criterion T_f of the PDC case is very close to that of the DC case. A possible reason is that a varying electric field promotes fluid motion. However, the PDC field has a minimal effect on the nonlinear criterion T_f.

Then, we examine the bifurcation process under the different frequencies of the PDC field to find the relationship between the bifurcation process and the frequency of PDC. Fig. 10(b) and (c) show the electroconvection bifurcation diagram when $f = 0.02$ and $f = 0.1$. We find that the linear criterion T_c increases with the frequency, which verifies the existence of a critical frequency. For the same T, the lower frequency voltage can promote fluid motion more than the higher frequency voltage. According to the results, we can calculate the average kinetic energy (26) as follows:

$$E_k = \frac{1}{2V_t}\int |\mathbf{u}|^2 dV = \frac{1}{2V_t}\sum_{k=1}^{N} |\mathbf{u}_k|^2 V_k = \frac{1}{2N}\sum_{k=1}^{N} |\mathbf{u}_k|^2 \tag{26}$$

where N represents the number of cells in our mesh and $V_t = NV_k$ for a uniform mesh.

The RMS of the average fluid kinetic energy for the PDC with $f = 0.02$ case is 1.153 and that of the PDC with $f = 0.1$ is 1.1014 when T ($T = 180$) is close to the linear criterion T_c. We also calculate the DC case for $T = 180$; its average kinetic energy is 1.066, which is lower than the values of the PDC cases for $f = 0.02$ and $f = 0.1$. When T increases, the fluid has more kinetic energy under low-frequency rather than high-frequency cases to support the fluid motion under the same external driving force. Therefore, we find that low-frequency cases have lower T_c values than high-frequency cases. The RMS of the average kinetic energy of the fluid for the PDC with $f = 0.02$ case is 0.4058 and that of the case for $f = 0.1$ is 0.4064 when $T = 120$, which is close to the nonlinear criterion T_f. From these results, we can infer that the average kinetic energy varies little as the PDC frequency increases when T is relatively low.

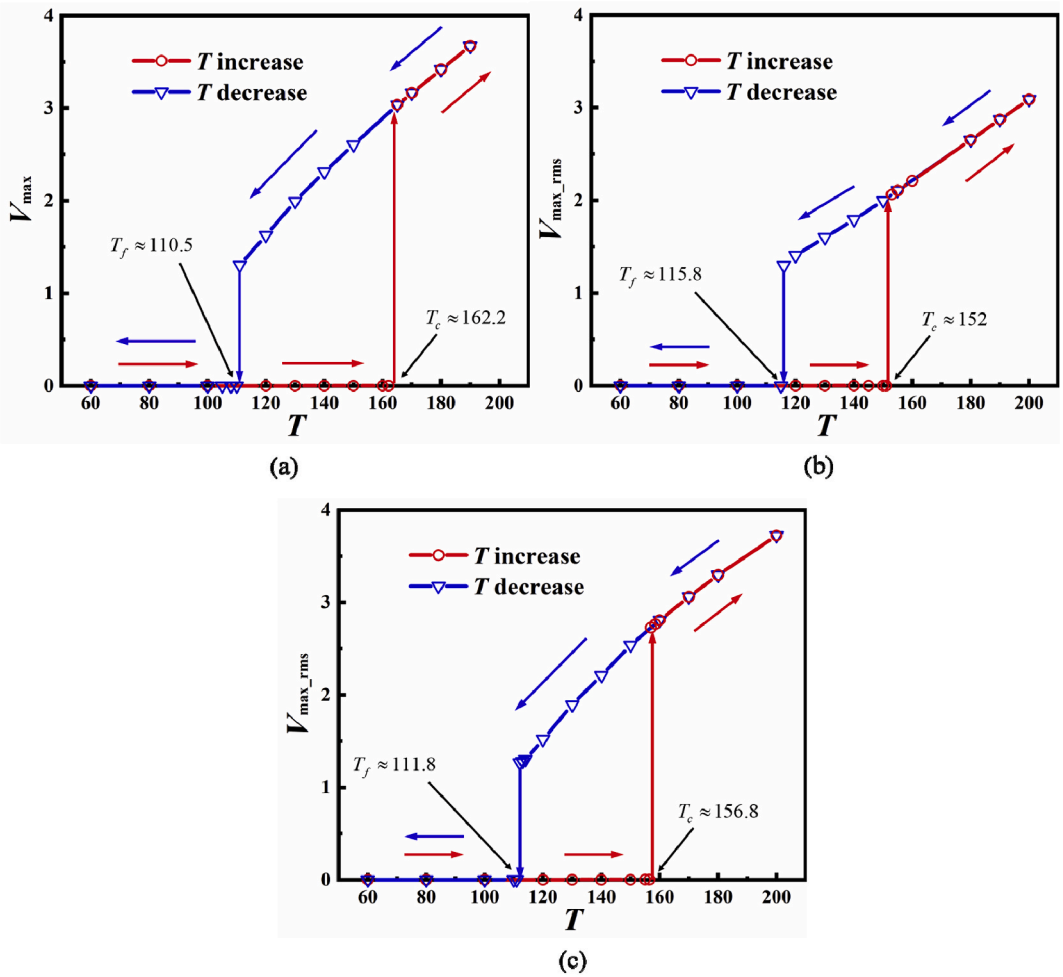

Fig. 10. Bifurcation diagram for $C = 10$, $M = 10$, and $\alpha = 1 \times 10^{-4}$; (a) direct current, (b) pulsed direct current (PDC; $f = 0.02$), and (c) PDC ($f = 0.1$).

However, the average kinetic energy decreases as the PDC frequency increases when T is relatively high. A possible reason is that higher frequency cases produce more viscous dissipation with the increase in driving parameter T.

We analyse the relationship between the frequency f of the PDC voltage and the oscillation frequency of the maximum velocity from Fig. 11. Based on the fast Fourier transform (FFT), the oscillation frequencies of the maximum velocity under PDC fields of $f = 0.02$ and $f = 0.1$ for $T = 190$ are 0.02 and 0.1, respectively. The results show that the frequency f of oscillation flow corresponds to the excitation period. The motion of the fluid is in a state of synchronous response [35].

3.2. *Stability for pure unipolar injection under an AC field*

We quantitatively measure the influence of the AC field on electroconvection and numerically validate two regimes: periodic ECF and inhibited ECF, which were explained theoretically in Section II B. We still select $C = 10$, which has been widely studied for the DC and PDC cases. A is still 0.614. In addition, 0.614 is half of the critical wavelength that has been verified in Fig. 4(b).

We provide numerical estimates to confirm the critical frequency of our system under AC fields. Fig. 12 shows the rms of maximum velocity V_{max} versus frequency for $T = 160$ and $T = 190$ under AC fields. We estimate the critical frequency $f_c = 0.0316$ for both the $T = 160$ and $T = 190$ cases, which is consistent with $1/t_T = 0.0316$.

3.2.1. *Periodic eletroconvective flow regime ($f < f_c$)*

First, we analyse a case with a moderately small AC frequency $f = 0.01$ ($f < f_c$). Fig. 13(a) shows the time series of charge density and streamline under half an oscillation. Fig. 13(b)–(c) shows the temporal evolution of the periodic voltages of AC and V_{max}. A similar observation as the PDC case can be made for this configuration when an AC is applied [Fig. 13(a)–(c)]. The difference is that the charge density distribution is reserved during the negative half-cycle because the opposite electrode becomes the injector. For $f < f_c$, the whole gap can be occupied with space charge, and we see that the void-charge region is formed periodically. A similar observation can be

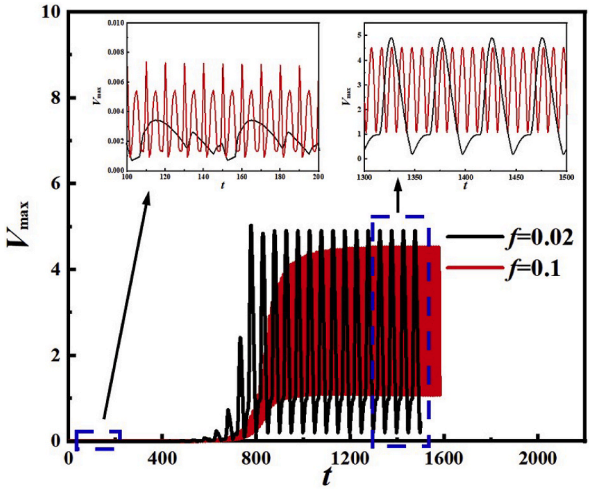

Fig. 11. Evolution of V_{max} ($C = 10$, $M = 10$, and $T = 190$) under the pulsed direct current field for $f = 0.02$ and $f = 0.1$.

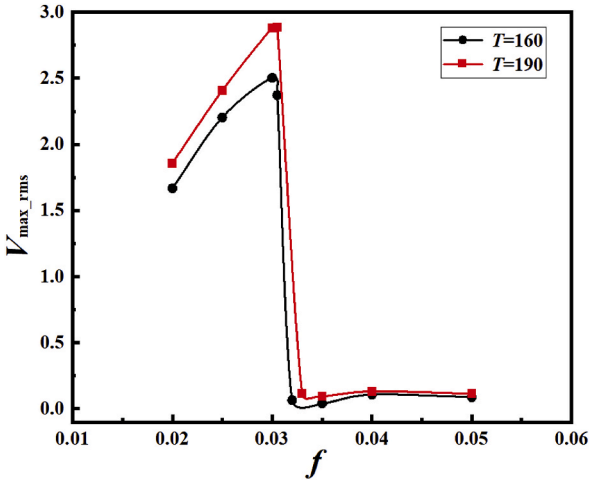

Fig. 12. RMS of maximum velocity V_{max} versus frequency for $T = 160$ and $T = 190$ under AC fields.

found during the negative half-cycle. The RMS of the maximum velocity under an AC electric field for $T = 160$ is 1.967, which is lower than 2.212, the corresponding RMS value under PDC voltage with the same frequency. The flow occurs through secondary bifurcation; two vortex structures and a central void-charge region appear in the fluid when $T = 190$ in Fig. 14(a–c).

Fig. 15 shows the subcritical bifurcation of AC electroconvection, where $T_c = 127.86$ and $T_f = 107.5$. We found that T_c in AC cases, 127.86, is lower than the 162.3 found in DC cases and T_f, 107.5, is slightly lower than the 110.5 found in DC cases. In AC cases, the periodic electric field promotes fluid motion. Thus, lower driving parameters are needed to maintain the charge-free region in the flow field. We also find that secondary bifurcation occurs in the fluid when $T = 190$ and that the critical value T_{c2} of the secondary bifurcation under DC ranges between 290 and 300 [68]. The AC field promotes subcritical bifurcation and secondary bifurcation.

3.2.2. *Inhibited eletroconvective flow regime ($f > f_c$)*

In this section, cases with AC frequencies greater than f_c are analyzed. The ECF instability induced by external DC fields demonstrates two vortex structures and void charge regions. Fig. 16(b) shows the evolution of the charge density for $f = 0.05$ ($f > f_c$) and $T = 170$ under the AC field. We find that the space charge is divided into two layers without overlap, and the fluid fluctuates periodically with low velocity [Fig. 16(a)]. Concurrently, there are obvious fluctuations in the charge layer [Fig. 16(b)]. Fig. 17(b) presents the evolution of the charge density and streamline diagram for $f = 0.05$ ($f > f_c$) and $T = 420$ under the AC field. The space charge remains in two layers with obvious fluctuations near the electrode, but the interface of the charge layer becomes more uneven than that seen for $T = 170$. Several irregular vortex flows appear in the fluid. At the same time, the irregular evolution of V_{max} fluctuates with time [Fig. 17(a)]. The cases for $T = 170$ and $T = 420$ fit well with the theoretical prediction in Section II. We also investigated electric Rayleigh cases

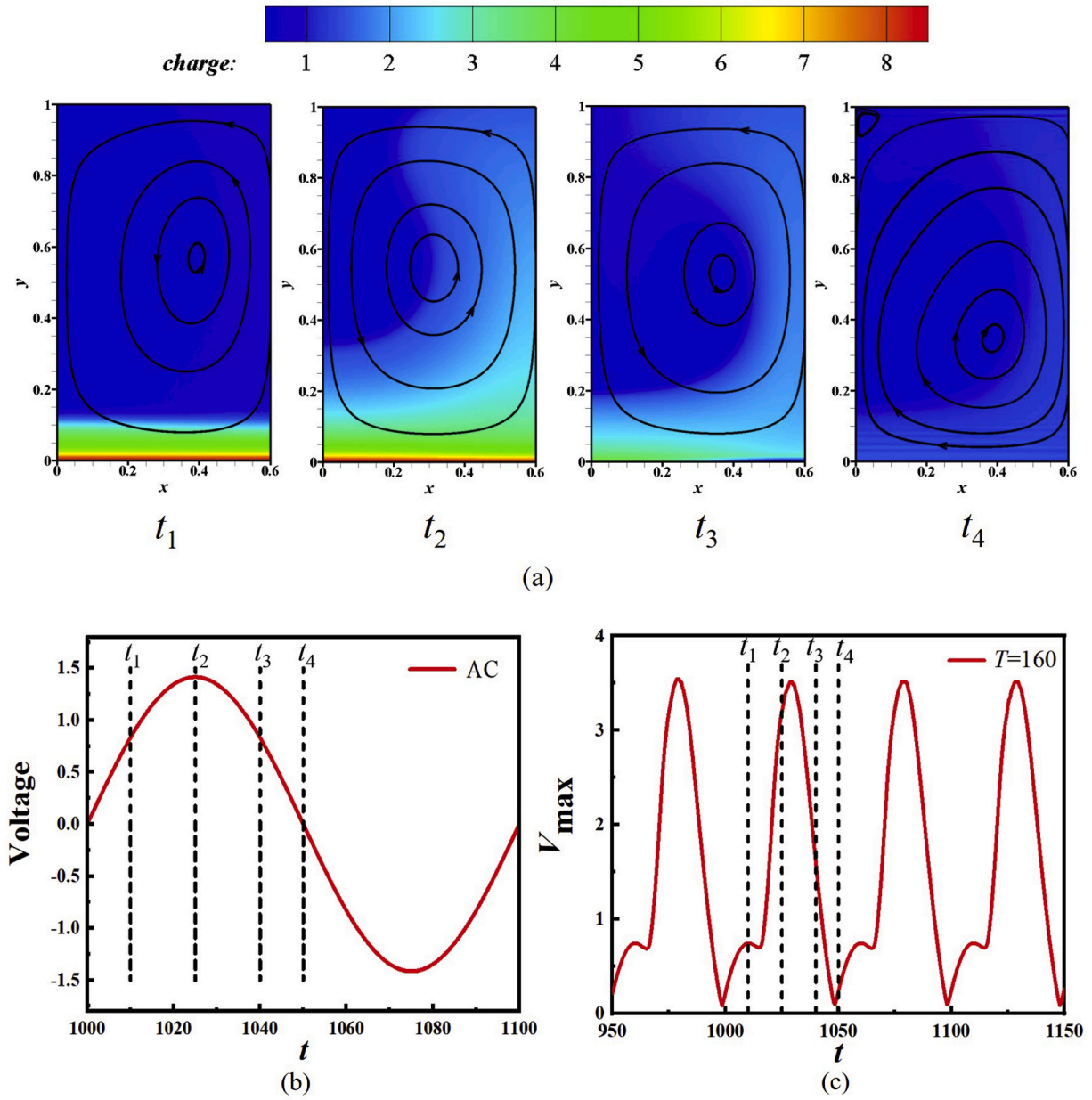

Fig. 13. Temporal evolution of charge density, q, distribution, voltage and V_{max} for $T = 160$ and $f = 0.01$, as a representation of the regular oscillation: (a) distribution of charge density and streamlines at four distinct times, (b) external periodic voltages of AC ($f = 0.01$) and (c) the periodic V_{max} signal.

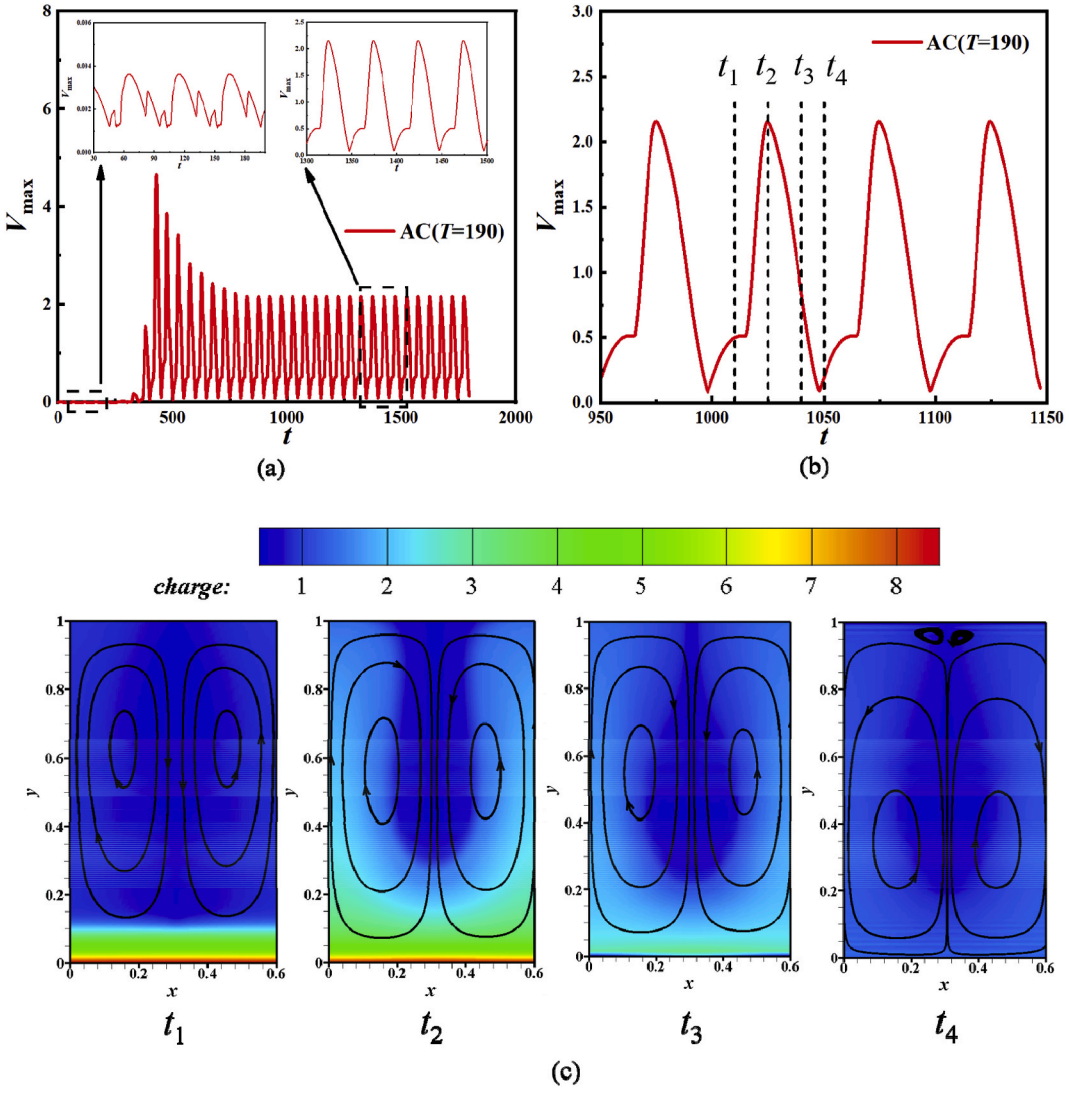

Fig. 14. Temporal evolution of voltage, V_{max}, charge density, q, distribution for $T = 190$ and $f = 0.01$, as a representation of the regular oscillation: (a) external periodic voltages of alternating current ($f = 0.01$), (b) the periodic V_{max} signal, and (c) distribution of charge density and streamlines at four distinct times.

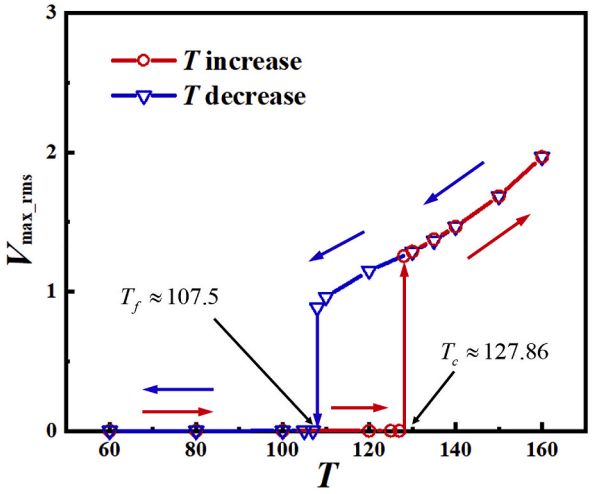

Fig. 15. Bifurcation diagram for $C = 10$, $M = 10$, and $\alpha = 1 \times 10^{-4}$ under an alternating current field when $f = 0.01$.

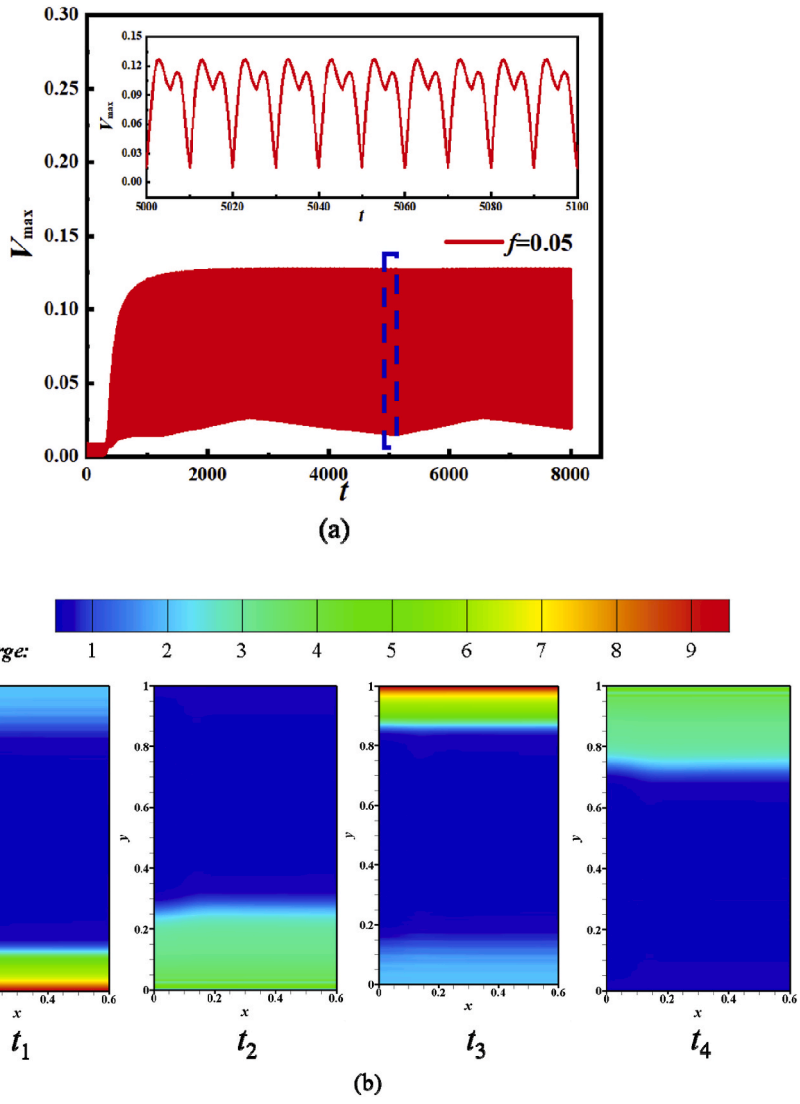

Fig. 16. (a) Evolution of maximum velocity for $T = 170$. (b) Evolution of the charge density when $f = 0.05$ under an alternating current field.

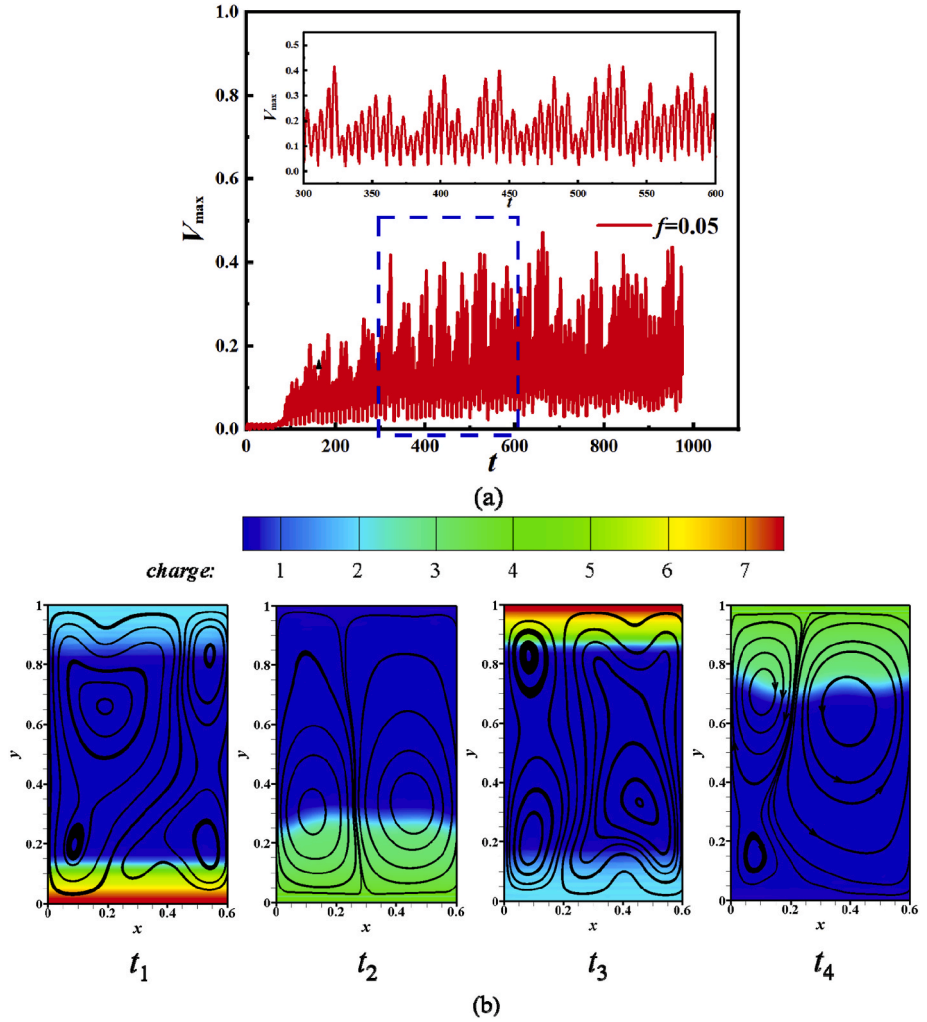

Fig. 17. (a) Evolution of maximum velocity for $T = 420$. (b) Evolution of the charge density and streamline when $f = 0.05$ under an alternating current field.

with larger T values, and Fig. 18(a and b) shows the corresponding results. The flow remains irregular for $T = 800$, and the velocity fluctuates more acutely than for $T = 420$ [Fig. 18(a)], leading to unsteady plume structures.

3.2.3. *Spectral analysis*

One way to look at the state of the flow is to compute the power spectral density (PSD) of the time series. Fig. 19 presents PSDs of V_{max} for $T = 160$ and $T = 420$ with different frequencies f of the AC field ranging from 0.01 to 0.05. When $T = 160$ for frequencies f from 0.01 to 0.03, the flow motion is typically periodic, and the amplitude of the fundamental frequency f_1 is consistent with the corresponding AC frequency f [Fig. 19(a)]. Moreover, for cases with frequencies f greater than the critical frequency, only periodic small disturbances occur in the fluid due to the significant decay of the PSD compared with the cases for $f = 0.01 - 0.03$ and $T = 160$ [Fig. 19(b)]. When $T = 420$ for frequencies f from 0.01 to 0.03, we can obtain similar results to $T = 160$ [Fig. 19(c)]. However, for $f = 0.04$ and 0.05, which are larger than the critical frequency, the flow becomes complicated and irregular, and the power spectrum shows obvious broadband characteristics [Fig. 19(d)]. From these results, we can see that the motion of the fluid is obviously in a state of synchronous response [35].

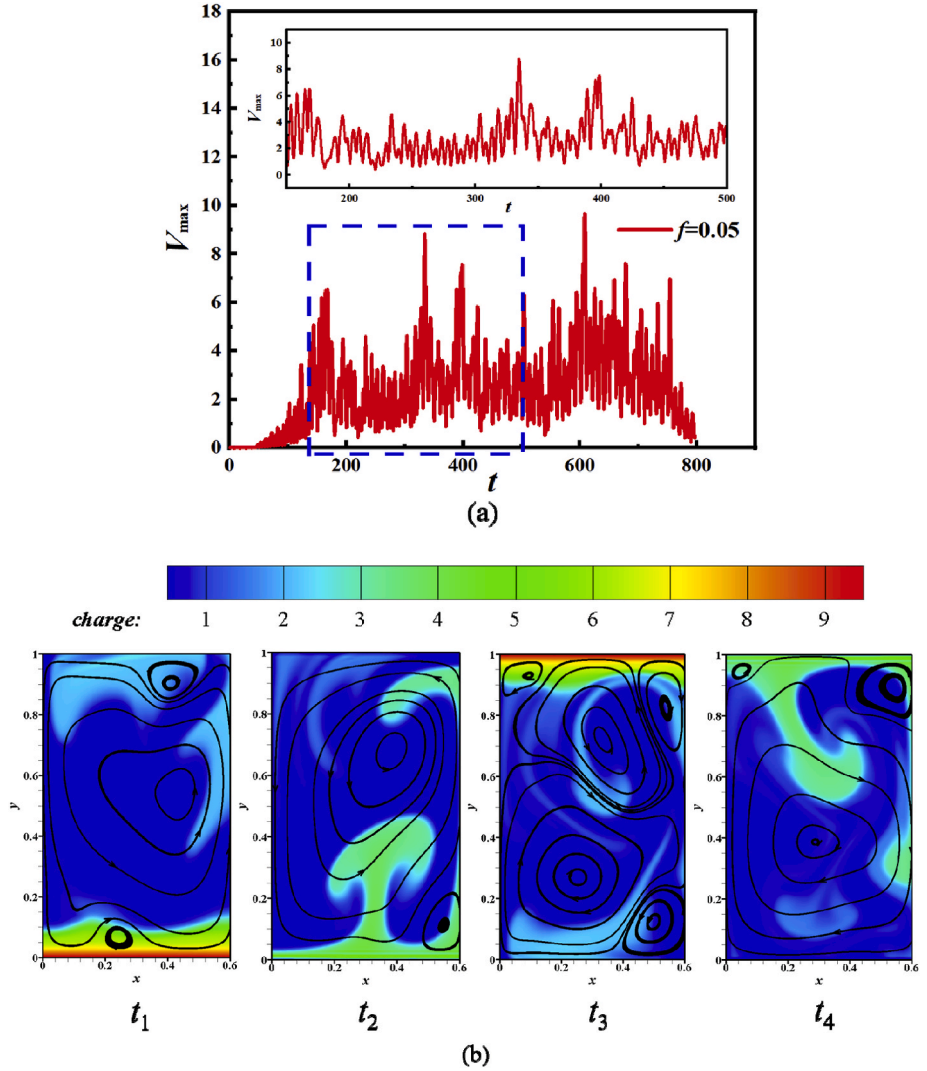

Fig. 18. (a) Evolution of maximum velocity for $T = 800$. (b) Evolution of the charge density and streamline when $f = 0.05$ under an alternating current field.

4. Conclusions

In this work, ECFs in a fluid layer enclosed by two parallel metal electrodes subjected to unipolar injection under PDC and AC fields are numerically investigated in detail by FVM. The PDC and AC waveforms are sinusoidal. The flow structures and bifurcation patterns have been studied in detail under various frequencies.

The results show that the varying electric fields play an essential role in instability patterns. The flow structures and linear and nonlinear criteria may change drastically with the field mode. In PDC cases, the flow loses its instability at the linear criterion T_c, and the bifurcation pattern is characteristic of subcritical bifurcation with hysteresis at different frequencies. The linear criterion T_c increases with increasing frequency f of the PDC field, while the nonlinear stability criterion T_f is hardly affected by the PDC field frequency. In AC cases, the periodic electroconvection flow regime and the inhibited electroconvection flow regime are noticed with an increase in the frequency of AC when the electric Rayleigh T remains constant. When the frequencies of AC are lower than the critical frequency $f_c = 0.0316$, the flow is in the periodic regime, and the bifurcation is characterized by subcritical bifurcation. When the frequency of AC is larger than the critical frequency f_c, the flow is in the inhibited regime.

At small electric Rayleigh, T, the flow is periodic with little disturbance, and the space charge remains in two layers near the electrode. The flow becomes irregular and enters a chaotic state when the electric Rayleigh T increases. The space charge layers near the electrode exhibit plume structures when T increases. In addition, the varying electric fields promote a transition from steady state

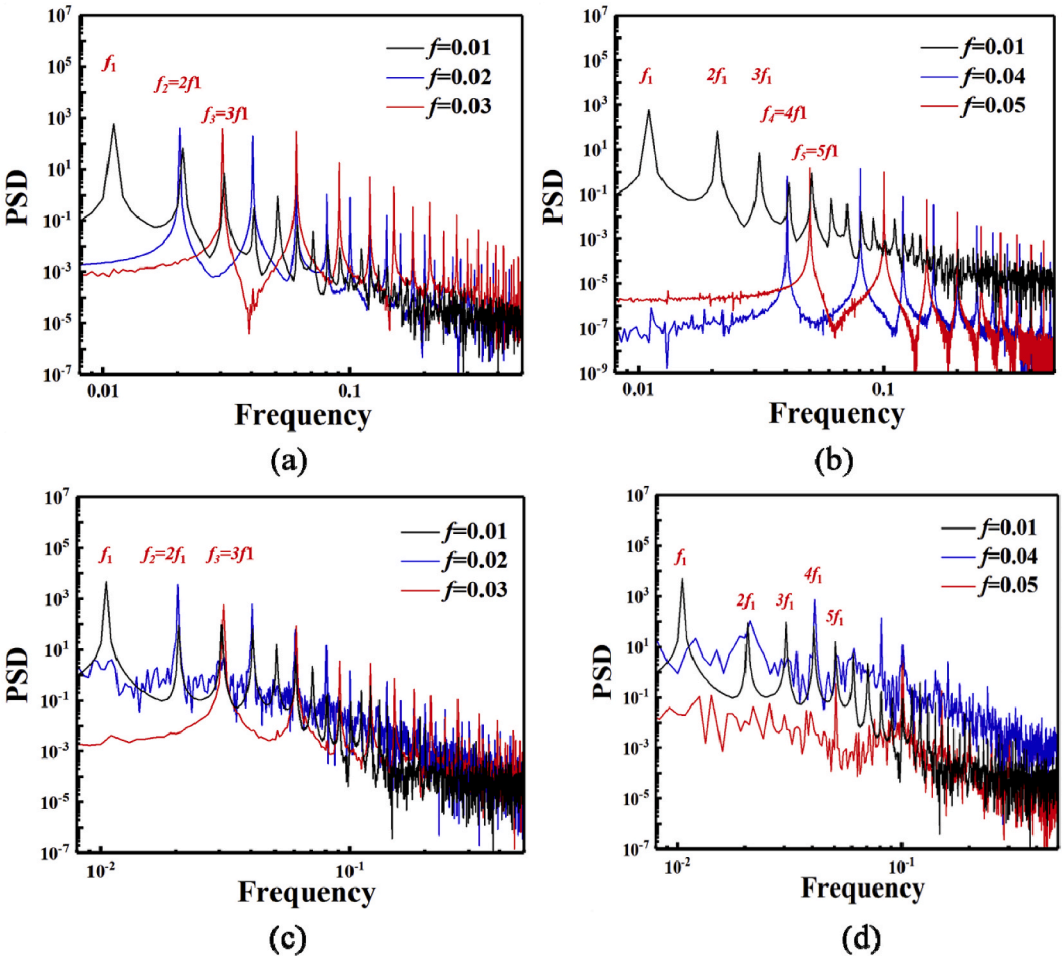

Fig. 19. Plot of power spectral density decay under alternating current fields: (a) $T = 160$ for $f = 0.01$, $f = 0.02$, and $f = 0.03$; (b) $T = 160$ for $f = 0.01$, $f = 0.04$, and $f = 0.05$; (c) $T = 420$ for $f = 0.01$, $f = 0.02$, and $f = 0.03$; (d) $T = 420$ for $f = 0.01$, $f = 0.04$, and $f = 0.05$.

to unsteady convection under PDC and AC fields. Therefore, AC-EHD systems operate at relatively lower voltage regimes than DC-EHD systems, making them suitable and safe for biological applications and portable systems. In the meantime, AC EHD can control fluid flow by selecting AC parameters (voltage and frequency f). Through a comprehensive comparison, the varying electric fields exhibit rich bifurcation and flow phenomena in ECFs.

In summary, the varying electric fields lead to unknown instability patterns and various dynamic structures in electroconvection that are not found when the DC field is considered. The interaction of alternating electric fields and fluid dynamics may have a potential impact on enhanced heat transfer because of enhanced or weakened oscillatory convection behavior. In future work, we plan to conduct experimental validation in a laboratory and its industrial applications. We will also extend our research to viscoelastic fluids or add thermal effects.

Data availability statement

The data that support the findings of this study are available from the corresponding author upon reasonable request.

Declaration of competing interest

The authors declare no conflicts of interest.

References

[1] C. Louste, Z. Yan, P. Traoré, R. Sosa, Electroconvective flow induced by dielectric barrier injection in silicone oil, J. Electrost. 71 (2013) 504.
[2] M. Wang, Q. Kang, Electrokinetic transport in microchannels with random roughness, Anal. Chem. 81 (2009) 2953.
[3] F. McCluskey, P. Atten, A. Perez, Heat transfer enhancement by electroconvection resulting from an injected space charge between parallel plates, Int. J. Heat Mass Tran. 34 (1991) 2237.
[4] J. Seyed-Yagoobi, Electrohydrodynamic pumping of dielectric liquids, J. Electrost. 63 (2005) 861.
[5] L. Wang, Z. Wei, T. Li, Z. Chai, B. Shi, A lattice Boltzmann modelling of electrohydrodynamic conduction phenomenon in dielectric liquids, Appl. Math. Model. 95 (2021) 361.
[6] R.K. Silva, S. Rauf, M. Dong, L. Chen, H. Bagci, K.N. Salama, 3D concentric electrodes-based alternating current electrohydrodynamics: design, simulation, fabrication, and potential applications for bioassays, Biosens. Bioelectron. 12 (2022) 215.
[7] R. Vaidyanathan, M.J. Shiddiky, S. Rauf, E. Dray, Z. Tay, M. Trau, Tunable “nano-shearing”: a physical mechanism to displace nonspecific cell adhesion during rare cell detection, Anal. Chem. 86 (2014) 2042.
[8] C.-H. Han, J. Jang, Integrated microfluidic platform with electrohydrodynamic focusing and a carbon-nanotube-based field-effect transistor immunosensor for continuous, selective, and label-free quantification of bacteria, Lab Chip 21 (2021) 184.
[9] S. Mishra, K.L. Barton, A.G. Alleyne, P.M. Ferreira, J.A. Rogers, High-speed and drop-on-demand printing with a pulsed electrohydrodynamic jet, J. Micromech. Microeng. 20 (2010), 095026.
[10] J. Plog, Y. Jiang, Y. Pan, A. Yarin, Electrostatic charging and deflection of droplets for drop-on-demand 3D printing within confinements, Addit. Manuf. 36 (2020), 101400.
[11] G.I. Taylor, Disintegration of water drops in an electric field, Ser. A: Math. Phys. Sci. 280 (1964) 383.
[12] J.S. Shrimpton, Electrohydrodynamics of charge injection atomization: regimes and fundamental limits, At. Sprays 13 (2003).
[13] Y.K. Suh, Modeling and simulation of ion transport in dielectric liquids-Fundamentals and review, IEEE Trans. Dielectr. Electr. Insul. 19 (2012) 831.
[14] P. Atten, J. Lacroix, B. Malraison, Chaotic motion in a Coulomb force driven instability: large aspect ratio experiments, Phys. Lett. 79 (1980) 255.
[15] P. Atten, Electrohydrodynamic instability and motion induced by injected space charge in insulating liquids, IEEE Trans. Dielectr. Electr. Insul. 3 (1996) 1.
[16] P. Traoré, A. Pérez, Two-dimensional numerical analysis of electroconvection in a dielectric liquid subjected to strong unipolar injection, Phys. Fluids 24 (2012), 037102.
[17] K. Luo, J. Wu, H.-L. Yi, H.-P. Tan, Lattice Boltzmann model for Coulomb-driven flows in dielectric liquids, Phys. Rev. E 93 (2016), 023309.
[18] N. Felici, Phénomenes hydro et aérodynamiques dans la conduction des diélectriques fluides, Rev. Gén. Electr. 78 (1969) 717.
[19] P. Atten, R. Moreau, Electrohydrodynamic stability of insulating liquids submitted to unipolar injection, J. Mec. 11 (1972) 471.
[20] J. Lacroix, P. Atten, E. Hopfinger, Electro-convection in a dielectric liquid layer subjected to unipolar injection, J. Fluid Mech. 69 (1975) 539.
[21] P. Atten, J. Lacroix, Non-linear hydrodynamic stability of liquids subjected to unipolar injection, J. Mec. 18 (1979) 469.
[22] A. Castellanos, P. Atten, Numerical modeling of finite amplitude convection of liquids subjected to unipolar injection, IEEE Trans. Ind. Appl. IA- 23 (1987) 825.
[23] R. Chicón, A. Castellanos, E. Martin, Numerical modelling of Coulomb-driven convection in insulating liquids, J. Fluid Mech. 344 (1997) 43.
[24] P. Vazquez, G.E. Georghiou, A. Castellanos, Characterization of injection instabilities in electrohydrodynamics by numerical modelling: comparison of particle in cell and flux corrected transport methods for electroconvection between two plates, J. Phys. D Appl. Phys. 39 (2006) 2754.
[25] P. Vázquez, G.E. Georghiou, A. Castellanos, Numerical analysis of the stability of the electrohydrodynamic (EHD) electroconvection between two plates, J. Phys. D Appl. Phys. 41 (2008), 175303.
[26] P. Vázquez, A. Castellanos, Numerical simulation of EHD flows using discontinuous Galerkin finite element methods, Comput. Fluids 84 (2013) 270.
[27] P. Traoré, A. Pérez, D. Koulova, H. Romat, Numerical modelling of finite-amplitude electro-thermo-convection in a dielectric liquid layer subjected to both unipolar injection and temperature gradient, J. Fluid Mech. 658 (2010) 279.
[28] B.-F. Wang, T.W.-H. Sheu, Numerical investigation of electrohydrodynamic instability and bifurcation in a dielectric liquid subjected to unipolar injection, Comput. Fluids 136 (2016) 1.
[29] K. Luo, J. Wu, A.T. Pérez, H.-L. Yi, H.-P. Tan, Stability analysis of electroconvection with a solid-liquid interface via the lattice Boltzmann method, Phys. Rev. Fluids 4 (2019), 083702.
[30] K. He, Z. Chai, L. Wang, B. Ma, B. Shi, Numerical investigation of electro–thermo-convection with a solid–liquid interface via the lattice Boltzmann method, Phys. Fluids 33 (2021), 037128.
[31] Z.Y. Zhang, T.F. Li, Z.G. Su, J. Wu, H.L. Yi, Instability of electroconvection in viscoelastic fluids induced by strong unipolar injection between two coaxial cylinders, Phys. Rev. Fluids 7 (2022).
[32] K. Luo, J. Wu, H.-L. Yi, H.-P. Tan, Three-dimensional finite amplitude electroconvection in dielectric liquids, Phys. Fluids 30 (2018), 023602.
[33] Z.-G. Su, Y.-M. Zhang, K. Luo, H.-L. Yi, Instability of electroconvection in viscoelastic fluids subjected to unipolar injection, Phys. Fluids 32 (2020), 104102.
[34] N.C. Roy, F. Yesmin, L.K. Saha, S. Siddiqa, Electrohydrodynamics natural convection flow of nanofluids in a rectangular cavity enclosed by a corrugated bottom surface, Fluid Dynam. Res. 53 (2021).
[35] B.L. Smorodin, A.V. Taraut, Parametric convection of a low-conducting liquid in an alternating electric field, Fluid Dynam. 45 (2010) 1.
[36] B.L. Smorodin, A.V. Taraut, Dynamics of electroconvective wave flows in a modulated electric field, J. Exp. Theor. Phys. 118 (2014) 158.
[37] V.D. Nguyen, D. Byun, Mechanism of electrohydrodynamic printing based on ac voltage without a nozzle electrode, Appl. Phys. Lett. 94 (2009), 173509.
[38] J. Kim, H. Oh, S.S. Kim, Electrohydrodynamic drop-on-demand patterning in pulsed cone-jet mode at various frequencies, J. Aerosol Sci. 39 (2008) 819.
[39] R. Vaidyanathan, S. Dey, L.G. Carrascosa, M.J. Shiddiky, M. Trau, Alternating current electrohydrodynamics in microsystems: pushing biomolecules and cells around on surfaces, Biomicrofluidics 9 (2015), 061501.
[40] A. Krekhov, W. Decker, W. Pesch, N. Eber, P. Salamon, B. Fekete, A. Buka, Patterns driven by combined ac and dc electric fields in nematic liquid crystals, Phys. Rev. E 89 (2014), 052507.
[41] S. Rudroff, H. Zhao, L. Kramer, I. Rehberg, Secondary instabilities form a codimension-2 point accompanied by a homoclinic bifurcation, Phys. Rev. Lett. 81 (1998) 4144.
[42] H. Jing, Y. Xiang, M. Xu, E. Wang, J. Wang, N. Éber, Á. Buka, Light-controllable electroconvection patterns in a chiral nematic liquid crystal, Phys. Rev. Appl. 10 (2018), 014028.
[43] M. Shiomi, E.-J. Choi, J.-H. Huh, Prewavy instability-originated dielectric chevrons of electroconvection in nematic liquid crystals, Phys. Rev. E 102 (2020), 042704.
[44] L.H. Olesen, M.Z. Bazant, H. Bruus, Strongly nonlinear dynamics of electrolytes in large ac voltages, Phys. Rev. E 82 (2010), 011501.
[45] R.F. Stout, A.S. Khair, Moderately nonlinear diffuse-charge dynamics under an ac voltage, Phys. Rev. E 92 (2015), 032305.
[46] J. Kim, S. Davidson, A. Mani, Characterization of chaotic electroconvection near flat inert electrodes under oscillatory voltages, Micromachines 10 (2019) 161.
[47] S.M. Davidson, M.B. Andersen, A. Mani, Chaotic induced-charge electro-osmosis, Phys. Rev. Lett. 112 (2014), 128302.
[48] V. Calero, R. Fernández-Mateo, H. Morgan, P. García-Sánchez, A. Ramos, Stationary electro-osmotic flow driven by AC fields around insulators, Phys. Rev. Appl. 15 (2021), 014047.
[49] P. Atten, B. Malraison, S.A. Kani, Electrohydrodynamic stability of dielectric liquids subjected to ac fields, J. Electrost. 12 (1982).
[50] B.L. Smorodin, G.Z. Gershuni, M.G. Velarde, On the parametric excitation of thermoelectric instability in a liquid layer open to air, Int. J. Heat Mass Tran. 42 (1999) 3159.
[51] B.L. Smorodin, M.G. Velarde, Electrothermoconvective instability of an ohmic liquid layer in an unsteady electric field, J. Electrost. 48 (2000) 261.
[52] O. Nekrasov, B. Smorodin, The electroconvective flows of a weakly conducting liquid in the external DC and AC electric fields, Microgravity Sci. Technol. 34 (2022).

[53] Z. Sun, D. Sun, J. Hu, P. Traoré, H.-L. Yi, J. Wu, Experimental study on electrohydrodynamic flows of a dielectric liquid in a needle-plate configuration under direct/alternating current electric field, J. Electrost. 106 (2020), 103454.
[54] A. Castellanos, Coulomb-driven convection in electrohydrodynamics, IEEE Trans. Electr. Insul. 26 (1991) 1201.
[55] L.M. Landau, E.M. Lifshitz, Electrodynamics of Continuous Media, Addison-Wesley, RM, Moscow, 1971.
[56] D. Nakhla, E. Thompson, B. Lacroix, J. Cotton, Measurement of heat transfer enhancement in melting of n-Octadecane under gravitational and electrohydrodynamics (EHD) forces, J. Electrost. 92 (2018) 31.
[57] A. Castellanos, in: A. Castellanos (Ed.), Conduction and Polarization, Electrohydrodynamics, Springer-Verlag, New York, 1998. Chap. 2.
[58] C. Druzgalski, M. Andersen, andA. Mani, Direct numerical simulation of electroconvective instability and hydrodynamic chaos near an ion-selective surface, Phys. Fluids 25 (2013), 110804.
[59] M. Abramowitz, E.I.A. Stegun, Handbook of Mathematical Functions, Dover Pub., Inc., New York, 1972, p. 375.
[60] V.K. Patel, F. Robinson, J. Seyed-Yagoobi, J. Didion, Terrestrial and microgravity experimental study of microscale heat-transport device driven by electrohydrodynamic conduction pumping, IEEE Trans. Ind. Appl. 49 (2013) 2397.
[61] F. Pimenta, M.A. Alves, Numerical Simulation of Electrically-Driven Flows Using OpenFOAM, 2018 arXiv preprint arXiv:1802.02843.
[62] M. Alves, P. Oliveira, F. Pinho, A convergent and universally bounded interpolation scheme for the treatment of advection, Int. J. Numer. Methods Fluid. 41 (2003) 47.
[63] M. Zhang, F. Martinelli, J. Wu, P.J. Schmid, M. Quadrio, Modal and non-modal stability analysis of electrohydrodynamic flow with and without cross-flow, J. Fluid Mech. 770 (2015) 319.
[64] Y. Guan, X. He, Q. Wang, Z. Song, M. Zhang, J. Wu, Monotonic instability and overstability in two-dimensional electrothermohydrodynamic flow, Phys. Rev. Fluids 6 (2021), 013702.
[65] Y.F. Guan, I. Novosselov, Two relaxation time lattice Boltzmann method coupled to fast Fourier transform Poisson solver: application to electroconvective flow, J. Comput. Phys. 397 (2019) 8.
[66] J. Wu, P. Traoré, A.T. Pérez, P.A. Vázquez, On two-dimensional finite amplitude electro-convection in a dielectric liquid induced by a strong unipolar injection, J. Electrost. 74 (2015) 85.
[67] X. Shan, Simulation of Rayleigh-Bénard convection using a lattice Boltzmann method, Phys. Rev. E 55 (1997) 2780.
[68] J. Wu, P. Traore, C. Louste, L. Dascalescu, F.-B. Tian, A.T. Perez, Effect of the mobility parameter on the oscillatory electroconvection of dielectric liquids subject to strong unipolar charge injection, IEEE Trans. Ind. Appl. 50 (2014) 2306.